Preparation of single-phase YbB$_6$ by low-temperature solid-state reaction method using iodine

Tuncay Simsek[1]

Abstract

In this study, low-temperature solid-state synthesis of pure nanocrystalline ytterbium hexaboride (YbB$_6$) employing iodine-based reduction method has been discussed. For the reduction reaction, the mechanically activated powder mixture of ytterbium oxide, boron oxide, magnesium, and iodine was heated up under Ar in a quartz tube to 85 °C. All reaction byproducts, viz. MgO, Mg$_3$(BO$_3$)$_2$, and YbI$_2$, were removed by hot acid leaching with 3 M HCl solution to form pure YbB$_6$. The morphological and phase structure of the synthesized YbB$_6$ powder were analyzed by X-ray diffractometry (XRD), high-resolution transmission electron microscopy (HRTEM), and Raman spectroscopy. The crystalline phases obtained were refined by multi-phase Rietveld refinement. XRD and Raman spectroscopy showed a contrast between the nano-YbB$_6$ formed by the present low-temperature iodine-based reduction method versus mechanochemical method. The YbB$_6$ produced by the low-temperature iodine reduction method is highly crystalline in nature, whereas YbB$_6$ produced by mechanochemical method is less crystalline or conversely more amorphous in nature. The iodine-based reduction method indeed played a definitive role to allow the reaction to take place at a lower temperature enabling the formation of nanocrystalline YbB$_6$.

Introduction

Rare-earth hexaborides (REB$_6$) are classified in the groups of materials of superior properties attracting the attention of many scientist and technologist recently. Their unique features such as high mechanical strength and thermal stabilities, low work function, high melting points, and low volatility at high temperatures make them potential candidates for the advanced technological applications [1–4]. Their unique electromagnetic properties have been drawing continued interest for a variety of engineering applications. These properties stem from their unique crystal structure characteristics. Their rigid crystal structure comprises cubical arrangements of metal atoms in a web of covalently bonded boron atoms. The unit cell can be described as a cube with boron octahedra occupying eight corners of the cube with a metal atom at the body-

center position. The metallicity of REB$_6$ depends on the valence of the metal atom in REB$_6$. For a bivalent metal, REB$_6$ behave as non-metallic, and for trivalent metals, REB$_6$ show metallic property since the third electron of the metal goes to the conduction band contributing to the electrical property of REB$_6$. The valence electrons of boron are spread over five bonds creating electron vacancy. For each unit cell of REB$_6$, this situation produces two-hole states for every B$_6$ group where each metal atom provides two electrons to fill the holes. These characteristics together with the strong bonds between the boron atoms in the crystal structure framework produce REB$_6$ that have electro-magnetic properties with high thermal stabilities [5]. Among all REB$_6$, YbB$_6$ is especially attractive for its relatively low density, high mechanical strength, and high melting point characteristics [6]. The crystalline form of YbB$_6$ has cubic Pm-3m space group symmetry like most of the rare-earth hexaborides (REB$_6$), resembling the crystal structure of CsCl. Rare-earth ion and octahedral B$_6$ occupy Cs site and Cl site respectively, and the octahedral B$_6$ cluster links to each other by strong covalent bonds providing high hardness characteristics [7–9]. Although the crystal structure of YbB$_6$ is similar to those of the other REB$_6$ compounds, the electronic structure of YbB$_6$ differs from those of the other

✉ Tuncay Simsek
  tuncaysimsek@kku.edu.tr

1 Department of Mechanical and Metal Technologies, Kırıkkale Vocational High School, Kırıkkale University, 71450 Kırıkkale, Turkey

group members. Sm and Yb are particularly known for their valence fluctuations principally in their hexaboride forms. For example, Sm atom occupies half-filled 4f shell, while Yb atom occupies fully filled 4f shell. The state of f-electrons determines the magnetic state of the Sm and Yb ions. At their higher valency states, the 5d electrons can be transferred to each other. The presence of strong covalently bonded boron octahedral clusters and different rare-earth metals influences the main properties of REB_6 [7]. The crystal structure of YbB_6 and the outer-shell electronic configurations of Yb and Sm are shown in Fig. 1 and Table 1 for comparison.

Several methods have been developed for the formation of YbB_6. The high-temperature floating zone, high-temperature sintering method, combustion synthesis method, and borothermal reduction studies were reported for the synthesis of YbB_6 [6, 10–12]. However, the biggest limitations of those methods are (a) the use of expensive elemental Yb and B powders, (b) the high cost of experimental setup, and (c) the requirement of high temperatures or pressures. Those studies were mostly concentrated on the synthesis of coarser structures, and very limited studies were reported about nanostructured YbB_6 until now [5, 9, 13]. The synthesis of YbB_6 in nanowire form was achieved at high-pressured medium at 240 °C in the autoclave after 12 h [5]. In another study, YbB_6 nanoparticles were obtained by solid-state metathesis reaction by reacting $YbCl_3.6H_2O$ and MgB_2 mixture at 650 °C for 1 h [9]. Recently, the synthesis of YbB_6 nanocrystals by mechanochemical method was reported that required 30 h of ball milling [13]. By virtue of long milling hours, these methods entrained undesired phases of impurity which required purification by washing or leaching with hot aqueous hydrochloric acid solutions.

Despite some modest efforts made in the past to synthesize YbB_6 at lower temperatures, e.g., 200–240 °C, the synthesis of nanosized YbB_6 happened to be very difficult because of high-temperature and harsher reaction condition requirements [8]. Reviewing all methods hitherto known, the present work appears to be the first of its kind to delineate the synthesis of YbB_6 nanoparticles below 100 °C by solid-state method. The YbB_6 nanoparticles were synthesized in ash furnace upon mechanically activating ytterbium oxide, boron oxide, magnesium, and iodine powder blend and then purifying the reaction product by leaching with HCl solution. The present work demonstrated a novel and viable method of synthesis for nanosized YbB_6 and it also opened the possibilities of
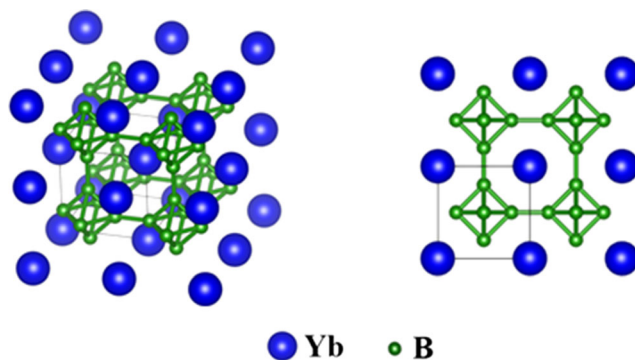

Fig. 1 Crystal structure of YbB_6

producing other related rare-earth hexaborides following the similar route. The phase structure and microstructural studies on the nanoparticles were analyzed by using XRD, Raman spectroscopy, and HRTEM. The crystal structures of as-synthesized and purified powders were also analyzed by using the multi-phase Rietveld refinement method. In this report, an important comparison has also been pointed out with respect to the morphologies of YbB_6 produced by the present low-temperature synthetic method versus the mechanochemical method. The XRD and Raman peak shifts revealed that the nanoparticles of YbB_6 produced by the present low-temperature method are highly crystalline in nature, whereas nanoparticles of YbB_6 produced by mechanochemical method are generally amorphous.

Experimental method

Yb_2O_3 (99.99%, Sigma Aldrich), B_2O_3 (98.00%, Eti Maden), I_2 (99.7%, Sigma Aldrich), and Mg (99.00%, Sigma Aldrich) were used as received. Both mechanical activation and solid-state reaction were carried out under high purity Argon (99.999%) to protect the powder blends and prevent surface oxidation from the contamination of atmospheric conditions. The flowchart for synthesizing YbB_6 is shown in Fig. 2. The Yb_2O_3, B_2O_3, I_2, and Mg powder blends are stoichiometrically weighed with a precision scale in the Ar-filled glovebox and kept in a tightly sealed hardened steel crucible to follow ball milling (Fritch, P6) for 2.5 and 4 h at 250 rpm using hardened steel balls as milling media. It is worth noting in this context that, prior to finalizing the milling conditions used, a series of runs were conducted to optimize the milling

RE ion	Shell	S (spin momentum)	L (orbital momentum)	J (total angular momentum)
$Yb^{2+}(Yb^{3+})$	$4f^{14}(4f^{13})$	0(1/2)	0(3)	0(7/2)
$Sm^{2+}(Sm^{3+})$	$4f^6(4f^5)$	3(5/2)	3(5)	0(5/2)

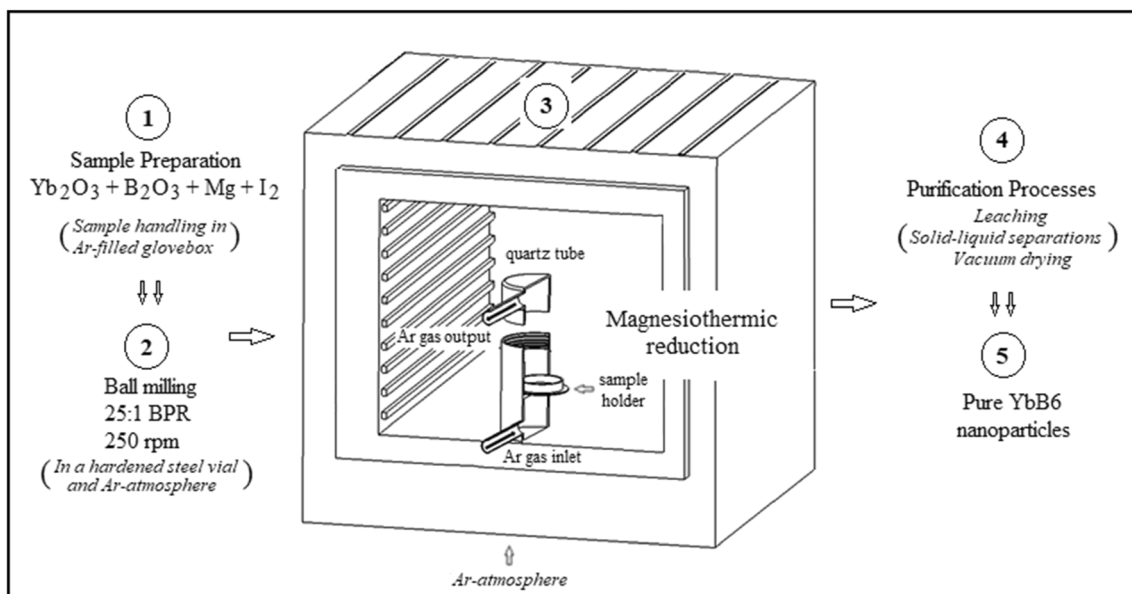**Table 1** The outer-shell electronic configurations of Yb and Sm

Fig. 2 Flowchart of synthesizing pure YbB_6

parameters for an efficient milling. Ball to powder ratio for milling was kept at 25:1. It was seen that rotating speed above 250 rpm caused iron (Fe) contamination due to waring from the milling media, whereas decreasing milling speed would cause longer milling period. In the latter case, the sample handling must be very carefully done under an inert atmosphere in order to avoid any unwanted oxidation reactions of the milled powders if exposed to air. Afterwards, powders were put in a quartz tube and followed by 30 min of gas flow through the tube and the temperature was slowly increased to 85 °C. The solid-state reaction of the powder mixture was conducted in an ash furnace by raising the temperature gradually at a rate of 2 °C/min. The reaction product was purified by treating with hot solution of 3 M HCl at 50 °C for an hour with magnetic stirring at 500 rpm. The powder to acid ratio used was 1 g:200 ml. The acid-washed powders were separated by centrifugation at 10,000 rpm for 20 min and washed several times with distilled water. For characterization, the washed precipitates were vacuum dried at 100 °C for 10 h in a vacuum oven (Memmert VO-400) with 20 mbar vacuum.

Particle size distribution of the initial materials was determined by a Malvern Mastersizer-2000 analyzer. The crystal structures of the synthesized powders were studied by using an X-ray diffractometer (Rigaku D/MAX-2200) at a scanning rate of 2° per minute for the angles ranging from 10° and 90° (2θ). To identify crystalline phases of the reaction products, the powder diffraction data files of the International Center for Diffraction Data (ICDD) were used. All morphological structures were evaluated using high-resolution transmission electron microscopy (HRTEM; Jeol 2100F). For HRTEM, the samples were prepared by suspending the powder in ethanol solution and sonicated for 30 min and then dried overnight on a HC300-Cu Holey carbon sample holder grid. Particle sizes

of the nano-powders were determined from the images obtained from TEM by image processing using ImageJ Analyzer software. Active vibrational modes of the YbB_6 were analyzed with a Raman spectrometer at 514 nm excitation wavelength (Renishaw in Via). The crystal structures of the synthesized phases were refined with Rietveld method using GSAS program [14]. Crystallography Open Database was used for the .cif files for the refinement. The background coefficients of the raw X-ray diffraction patterns were determined following the Sonneveld method [15]. For refinement, the scale factor and background coefficients were considered first prior to including the other parameters. The coefficients of the ninth-order polynomial function were refined with a few iterations until a good background fit is obtained. In the second step, peak positions and volume of the model structure were optimized and the zero offset and lattice parameters were refined. Pseudo-Voigt function was used for the peak profiles. For the refinement of powder patterns, $K\alpha_1$ and $K\alpha_2$ peaks are well separated at higher angles (low FWHM). The refined intensity ratio, $K\alpha_1/K\alpha_2$, in GSAS was ~ 2 using the integrated areas under the corresponding doublets. The mean particle size of the obtained YbB_6 phase was calculated using the isotropic Lorentzian Scherrer particle broadening parameter (LX) of refined peak profiles [14].

Results and discussion

The SEM images and XRD patterns of the initial powders are presented in Figs. 3 and 4. SEM images of the initial materials reveal the irregular morphology of Yb_2O_3 and B_2O_3, nearly spherical form and morphology of Mg and flat, and irregular shape of I_2. However, it is worth mentioning that I_2 could

Fig. 3 SEM images of initial materials. **a** Yb_2O_3. **b** Mg. **c** B_2O_3. **d** I_2
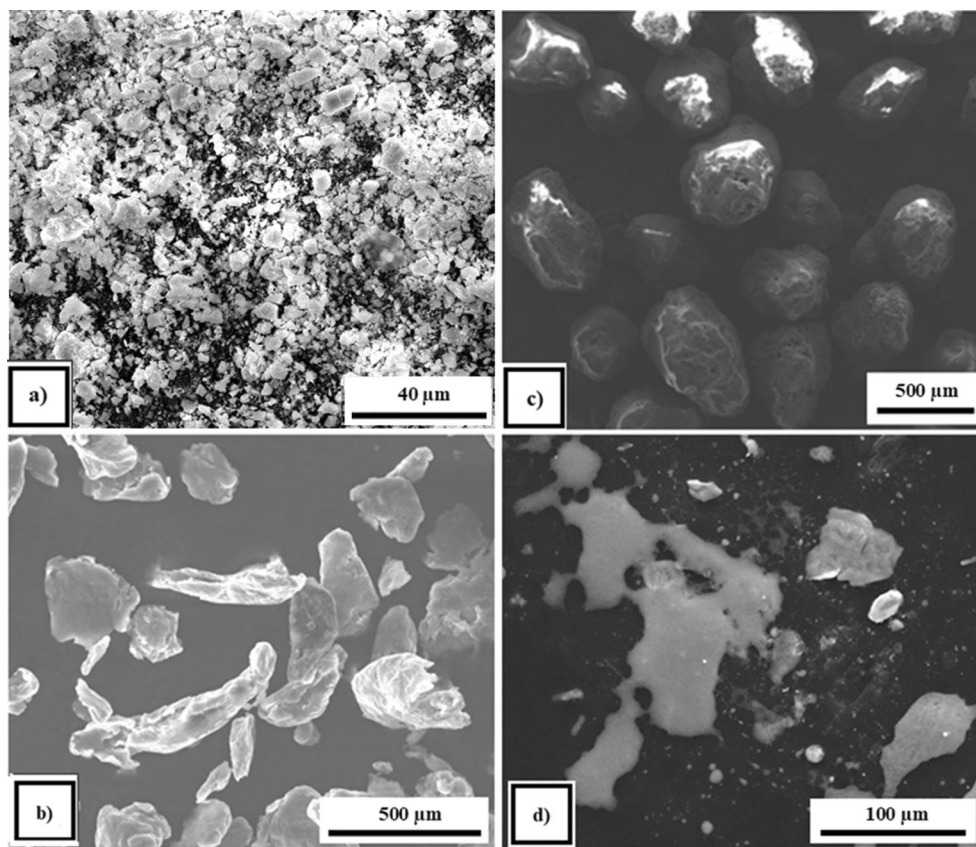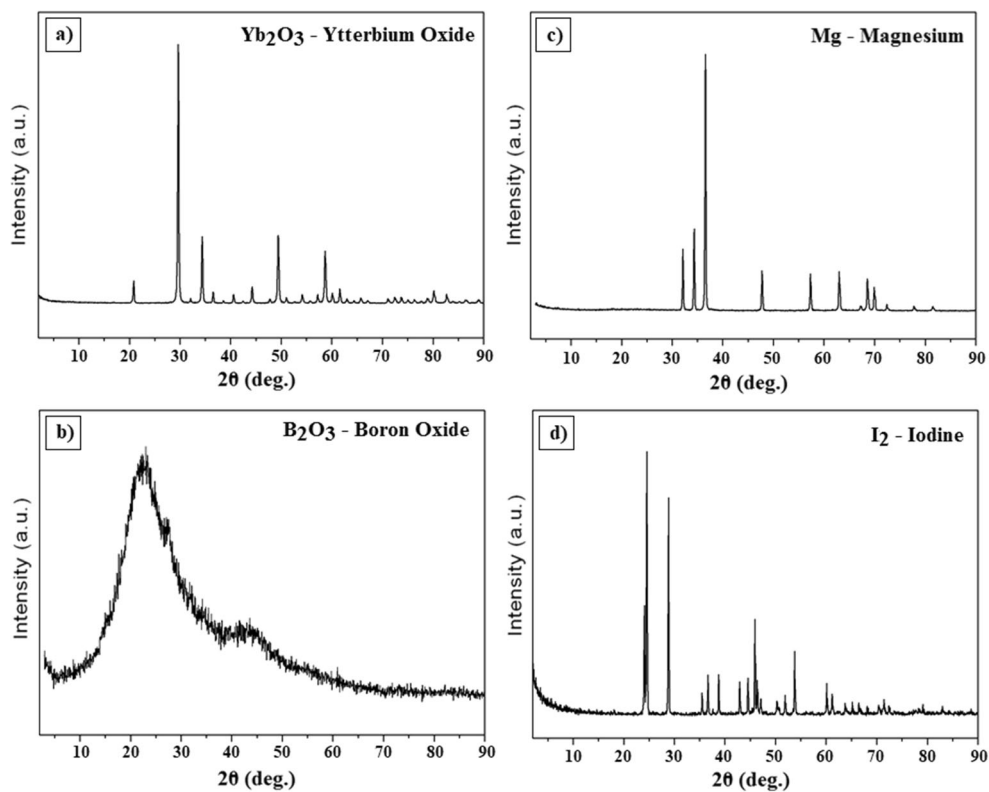

Fig. 4 XRD pattern of initial materials. **a** Yb_2O_3. **b** Mg. **c** B_2O_3. **d** I_2

oxidize very fast and its color could change to brown during sample preparation if exposed to air.

The XRD peak intensities of Yb_2O_3 (ICDD card no.: 03-065-3173), Mg (ICDD card no.: 01-089-5003), and I_2 (ICDD card no.: 00-043-0304) are shown in Fig. 4. The peak intensities could easily identify each of the crystalline initial materials, viz. Yb_2O_3, Mg, and I_2. However, B_2O_3 because of its amorphous structure appeared as an indiscrete noisy hump because of its amorphous nature and XRD peaks for B_2O_3 could not be identified.

Figure 5 shows the particle size distribution of the Yb_2O_3 (Fig. 5a), Mg (Fig. 5b), and B_2O_3 (Fig. 5c) initial powders with the d (0.5) values 0.5 μm, 137.5 μm, and 597.9 μm, respectively. The particle size distribution of Yb_2O_3 shows three modes, with peak maxima at 0.5 μm, 3.0 μm, and 200 μm. This could probably be due to the uncontrolled

particle clustering of the primary Yb_2O_3 particles. Mg and B_2O_3 powders had narrow size distributions. Particle size distribution of I_2 was not measured due to its coarser irregular grain sizes but microscopic investigation revealed particle sizes ranging between 60 μm and 1 mm (Fig. 3d).

In the typical synthesis, 0.28 g of Yb_2O_3, 0.74 g of Mg, 1.06 g of I_2, and 0.58 g of B_2O_3 were weighed in an Ar-filled glove box and put in a vial. Then, the powder mixtures were milled separately for 2.5 and 4 h under Ar and evaluated if there was any effect on the duration of milling. Figure 6a shows the XRD images of the powder mixtures before and after milling for 2.5 and 4 h. As seen from Fig. 6a, after ball milling the peak intensities of Yb_2O_3 (ICDD card no.: 03-065-3173, Bravais lattice: cubic, space group: Ia-3), Mg (ICDD card no.: 01-089-5003, Bravais lattice: hexagonal, space group: $P63/mmc$), and I_2 (ICDD card no.: 00-043-0304,

Fig. 5 Particle size distribution of the initial powders of **a** Yb_2O_3, **b** B_2O_3, and **c** Mg
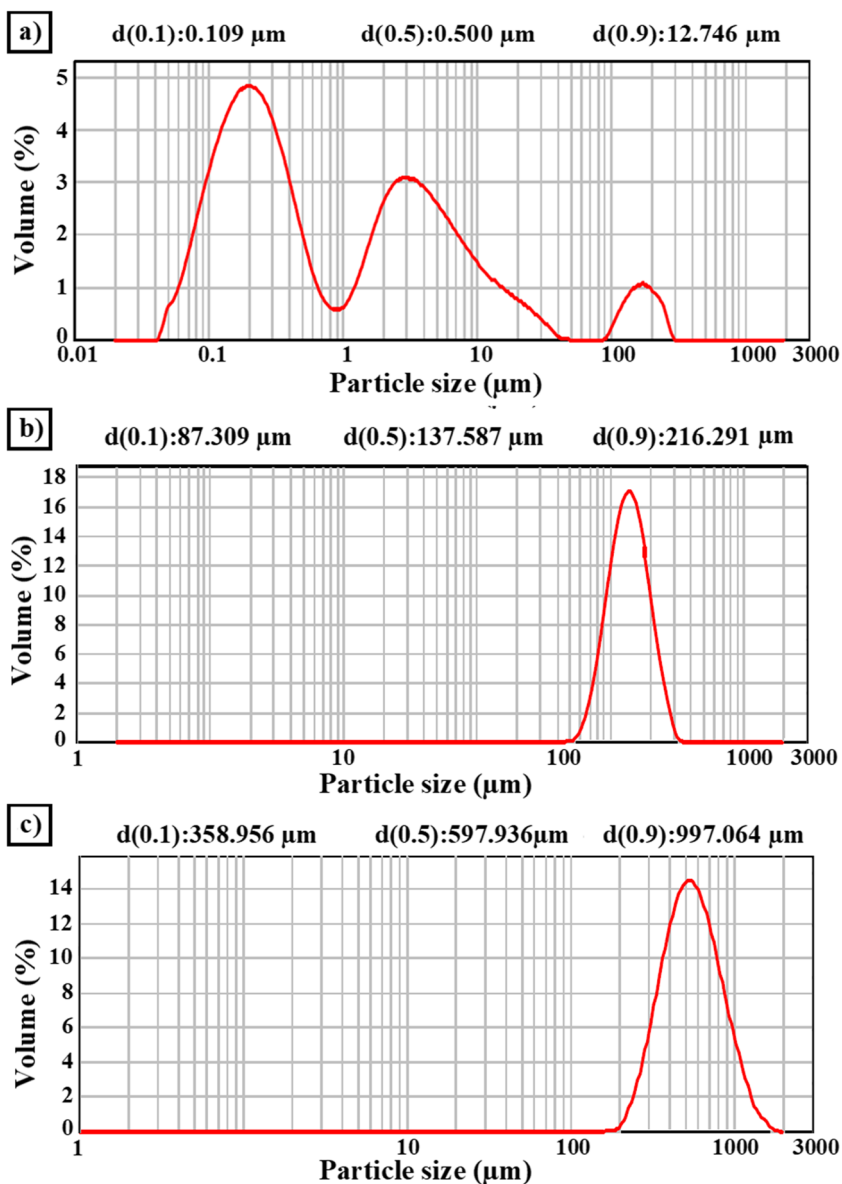
Bravais lattice: orthorhombic, space group: *bmab*), decreased and the area underneath expanded. This indicated the refinement of the grain sizes of the initial materials. The mean crystallite size and lattice strain of Yb_2O_3 and Mg before and after ball milling were calculated according to the Williamson-Hall method (1) [16] and the values are given in Table 2.

$$Bcos\theta = \frac{(K\lambda)}{D} + \varepsilon sin\,\theta \tag{1}$$

where θ is the Bragg angle, B is the full-width at half-maximum (FWHM) of the diffraction peak, K is a constant whose value is 0.9, ε is the internal microstrain, λ is the wavelength of the X-ray, and D is the crystallite size. The crystallite sizes and lattice strains calculated for Yb_2O_3 and Mg are given in Table 2. As it can be noticed, the reduction in crystallite sizes and increase in lattice strains occurred significantly with the increase in milling time. By increasing milling time, as it appeared from the XRD peak broadening of Yb_2O_3 and Mg, there was a gradual shift from the crystalline to the amorphous state of Yb_2O_3 and Mg. By virtue of creating lattice strains during the size refinement process by milling, the reactivity of powders also increases due to continuous deformation that the particles go through [17–19]. It is also to be noted that I_2 underwent amorphization very fast. Similar results were reported by Balcı et al. for synthesis of NbB_2/NbC mixtures [20]. They reported that ball milling processes resulted into increased surface area of powders with high activity and high reactivity caused for concurrent reaction mechanism. The occurrence of two reactions in one step affected the overall reactions that enabled reduction of reaction temperatures of milled powders. According to Balci, the milling period was not extended more than 4 h to avoid formation of any undesired phases. It is known that longer milling hours cause contaminations to the product. Regardless of the type of vial used, the waring of the vial is inevitable depending on the duration of milling [17], [20–22]. To avoid in any contamination and other microstructural changes, considering shorter milling hour should be beneficial for mechanical activation [19, 20].

Table 2 The changes in the crystallite size and lattice strain as calculated from Eq. 1 for Yb_2O_3 and Mg powders with the milling time

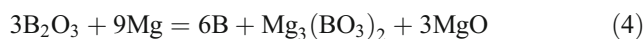| Milling period (h)	Crystallite size (nm)		Lattice strain [%]	
	Yb_2O_3	Mg	Yb_2O_3	Mg
0	52	64	0.241	0.301
2.5	37	46	0.314	0.373
4	29	23	0.470	0.515

The reduction reaction mechanism of YbB_6 with Yb_2O_3, B_2O_3, Mg, and I_2 powder mixture as per the conventional thoughts is given in Eq. 2.

$$Yb_2O_3 + 6\,B_2O_3 + 22\,Mg + I_2$$
$$= 2\,YbB_6 + 21\,MgO + MgI_2 \tag{2}$$
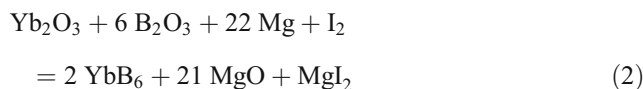
XRD patterns of the as-prepared and purified YbB_6 powder after removing the reaction byproducts are shown in Fig. 6b. From the XRD, it is, however, noticed that the as-prepared powders were actually comprised of YbB_6 (ICDD card no.: 03-065-1829), $B_2Mg_3O_6$ (ICDD card no.: 01-073-1541), MgO (ICDD card no.: 01-075-1525), and YbI_2 phases. Therefore, from the XRD data, the correct reaction mechanism must be as per Eq. 3.

$$2\,Yb_2O_3 + 24\,Mg + 2I_2 + 8\,B_2O_3$$
$$= 2\,YbB_6 + 2\,YbI_2 + 2\,Mg_3(BO_3)_2 + 18\,MgO \tag{3}$$
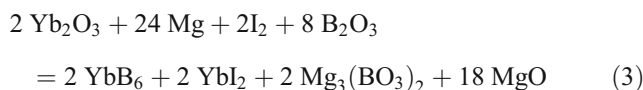
The step-by-step reduction reaction process is given in the following equations (Eqs. 4–7):

$$3B_2O_3 + 9Mg = 6B + Mg_3(BO_3)_2 + 3MgO \tag{4}$$

$$2Yb_2O_3 + 6Mg = 2\,Yb + 6\,MgO \tag{5}$$

$$Yb + I_2 = YbI_2 \tag{6}$$

$$YbI_2 + 6B = YbB_6 + I_2 \tag{7}$$

The Gibbs free energy indicates that the reactions in Eq. 3 are highly exothermic (ΔH − 2000 kjmol) and thermodynamically spontaneous (ΔG − 1900 kjmol) [5]. It is likely that Mg reduces B_2O_3 first to form B atoms, MgO, and an intermediate $B_2Mg_3O_6$ phases. Mg also reduces Yb_2O_3 to form Yb atom simultaneously (Eqs. 4 and 5). At the second step, Yb reacts with I_2 to form YbI_2 (Eq. 6). YbI_2 is an important intermediate for the formation of YbB_6. At the last step, the free B and YbI_2 react to yield YbB_6 releasing I_2 (Eq. 7). The crystal structures of phases formed during the experiments are given in Table 3. Wang et al. also reported I_2 assisted synthesis route for La, Ce, Pr, Nd, Sm, and Eu hexaborides. The synthesis of nanocubes of those hexaborides with mean size ranging between 450 and 700 nm was achieved at 170–250 °C. Wang et al. also emphasized that the crucial role of I_2, which formed MI, MOI

Fig. 6 a XRD pattern of initial materials for unmilled, 2.5-milled, and 4 h-milled powder mixture. **b** XRD graphs of the powders obtained after the instantaneous solid-state reaction of the reactant mixture at 85 °C, and after purifying the product, YbB_6, by hot HCl leaching
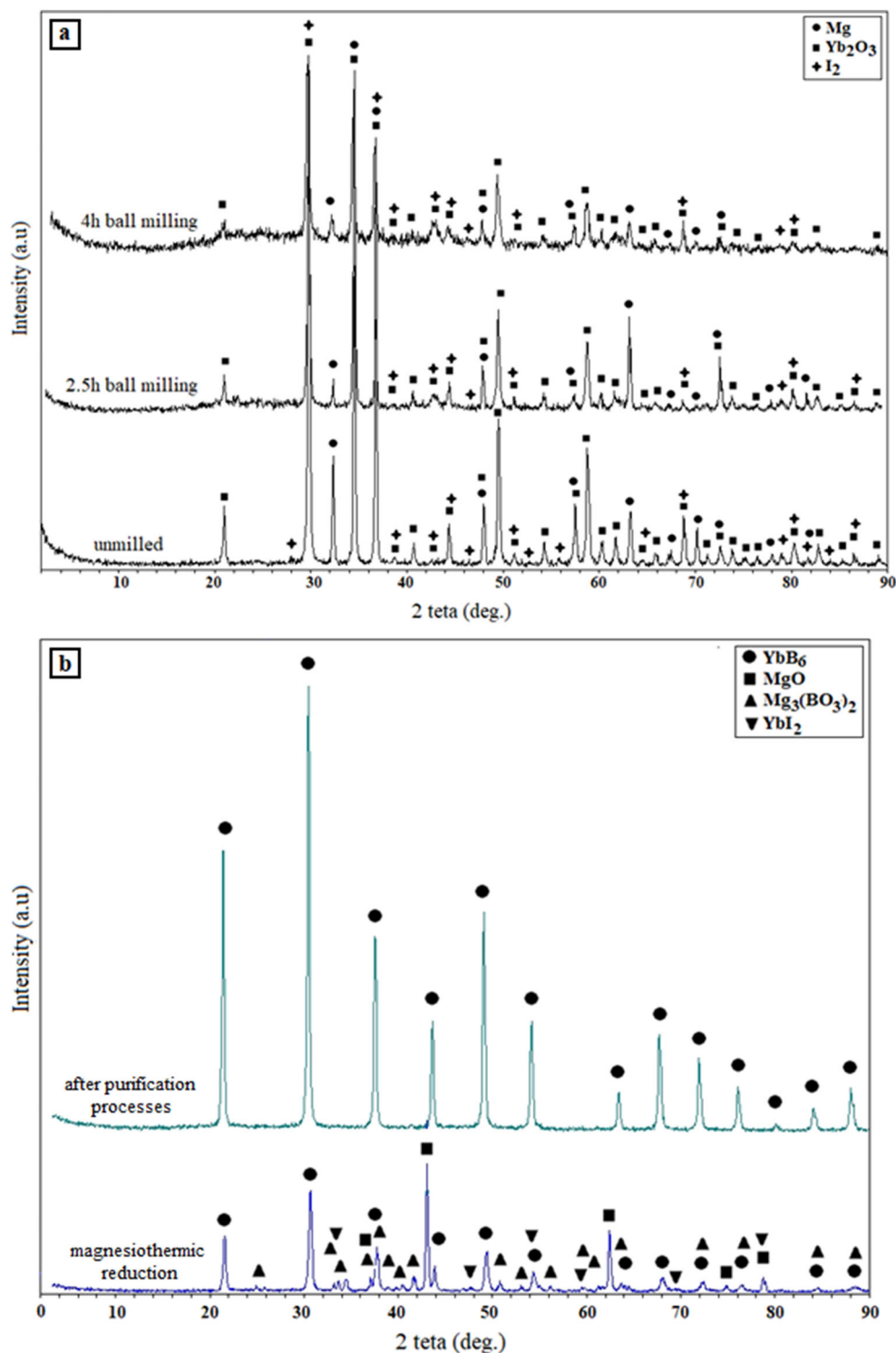
(where M is either La, Ce, Pr, Nd, or Sm), or similar intermediates, was for its quasi-catalytic function for the synthesis of hexaborides [23]. It was revealed that MB_6 could not be obtained even at 650 °C in the absence of I_2. In the studies of Han et al., the similar synthesis mechanisms were reported by high-pressure solid-state method. They indicated that I_2 was a vital intermediate for the formation of MgI_2 and YbI_2. They stated that MgI_2 promoted the crystallization of YbB_6, while YbI_2 played an important role as a powerful and versatile reducing agent [5].

To investigate detailed crystal structures of as-synthesized powders, Rietveld refinement was carried out as shown in Fig. 7. Table 3 gives the Wyckoff positions of obtained phases.

Table 3 Wyckoff positions of the reaction product phases obtained as shown in Eq. 3

Phase content	Atomic parameters	Uiso	Space groups
YbB$_6$	Yb 1a (0, 0, 0)	0.0045(3)	Pm-3m
	B 6f (0.224(3), 0.500, 0.500)	0.0076(2)	
MgO	Mg 4a (0, 0, 0)	0.0054(5)	Fm-3m
	O 4b (0.500, 0.500, 0.500)	0.0055(2)	
B$_2$Mg$_3$O$_6$	Mg1 2a (0, 0, 0)	0.0024(4)	Pnmn
	Mg2 4f (0.000, 0.313(2), 0.500)	0.0048(2)	
	B 4 g (0.253(2), 0.000, 0.548(2))	0.0017(2)	
	O1 4g (0.325(3), 0.000, 0.258(3))	0.0066(3)	
	O2 8h (0.210(5), 0.142(3), 705(4))	0.0071(5)	
YbI$_2$	Yb 1a (0, 0, 0)	0.0076(3)	P-3m1
	I 2d (0.341(2), 0.670(4), 0.922(2))	0.0045(3)	

The multi-phase Rietveld refinement results of the obtained phases are given in Fig. 7a. The observed XRD patterns of the experimental data are presented in red plus and the calculated patterns of the modeled structure are presented in black line (Fig. 7). Calculated Bragg reflections were plotted by vertical bars, while the difference between the two patterns is plotted in the lower part of the figure as a solid trace. The refined 2θ range was between 10 and 90°. The determination of the optimized structural parameters and relative phase fractions of phases obtained was achieved following the technic of multi-phase Rietveld refinement. The summary of crystallographic data and S (χ^2 goodness of fit) obtained by Rietveld refinement is given in Table 4. The relative percentages of YbB$_6$, B$_2$Mg$_3$O$_6$, MgO, and YbI$_2$ were determined as ~ 58%, ~ 26%, ~ 11%, and ~ 5%, respectively (Fig. 7a). Rietveld refinements of the purified samples of YbB$_6$ confirmed cubic structure in Pm-3m (221) space group with lattice parameters of $a = b = c = 4.143$ Å (Fig. 7b). The well-defined XRD peaks of the purified product were found to be consistent with the findings reported in the literature [6, 9, 24]. The isotropic Lorentzian Scherrer particle broadening parameter (X) of refined peak

profiles was used, as shown in Eq. 8, to calculate the average particle size of the purified YbB$_6$. As per Eq. 8, the average particle size (p) was determined as 96 ± 4 nm.

$$p = \frac{18000K\lambda}{\pi X} \tag{8}$$

where K is the Scherrer constant, X is the isotropic Lorentzian Scherrer particle broadening parameter, and λ is the wavelength.

Microstructural characterization of the purified YbB$_6$ nanoparticles was carried out by using HRTEM. The high-resolution images are given in Fig. 8a–d. It can be seen from Fig. 8 that the powders are composed of both irregular shaped particles and nano-cubes. The average particle size was about 121 ± 5.0 nm. The similar morphologies were observed in the study of Zhang et al. They reported the synthesis of LaB$_6$ nano-cubes with an average particle size of 200 nm by using LaCl$_3$ and B$_2$O$_3$ in autoclave at 500 °C for 4 h [25]. The high-resolution micrograph observations are also consistent with the average particle size calculated by the XRD technique (the average particle size was about 96 ± 4 nm nm). It can be
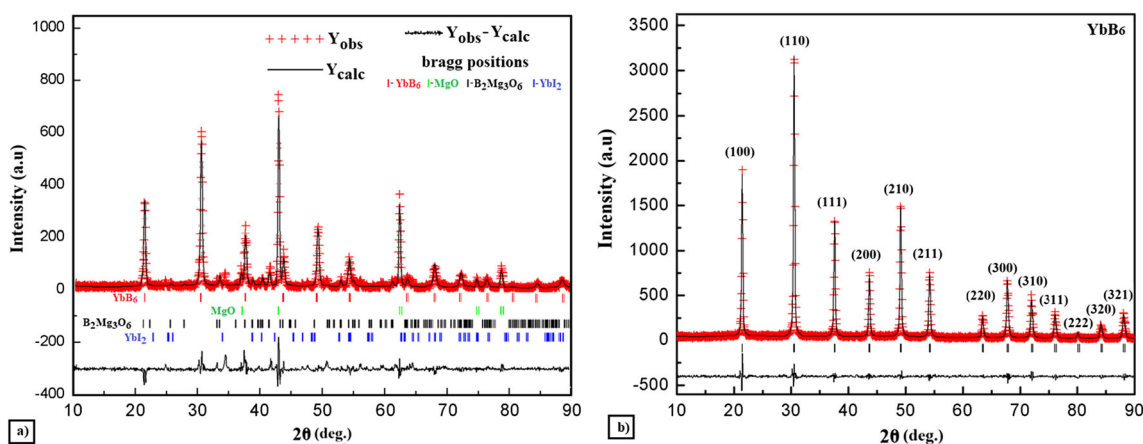

Fig. 7 **a** Multi-phase Rietveld refinement of powder mixture obtained after magnesiothermic reductions. **b** Single-phase Rietveld refinement of the purified YbB$_6$ nanoparticles

Table 4 Crystallographic data of as-synthesized mixtures by Rietveld refinement

Phase content	Phases obtained after magnesiothermic reductions				After purification
	YbB$_6$	MgO	B$_2$Mg$_3$O$_6$	YbI$_2$	YbB$_6$
Phase fraction (%)	58	26	11	5	100
Crystal system	Cubic	Cubic	Orthorhombic	Hexagonal	Cubic
a (Å)	4.141(2)	4.216(2)	5.410(4)	4.479(2)	4.143(3)
b (Å)	= a	= a	8.404	= a	= a
c (Å)	= a	= a	4.508	6.960	= a
Cell volume (Å3)	71.18(4)	73.99(2)	203.80(2)	120.82(5)	71.20(2)
S (χ^2)	2.152				1.401
Rp	0.181				0.089
Rwp	0.250				0.136
Data points	1739				1499

noticed that the average particle size estimated from XRD is generally lower than the particle size determined from TEM [26]. Since a particle may comprise several crystallites, the size of a particle is ought to be greater than the crystallite size. The synthesized YbB$_6$ powder particles are polycrystalline in nature. Each powder particulate is composed of many crystallites of varying sizes and orientations. TEM images reveal the presence of individual crystallites within the relatively larger powder particle sizes. To measure individual crystallite size from XRD happens to be a well-known technic. The HRTEM images present some dark and bright regions, which can be attributed to the orientation variations (Bragg contrast) and mass-thickness differences [27, 28].

Raman scattering spectra of purified YbB$_6$ nanoparticle obtained at room temperature with 514 nm excitation are given in Fig. 9b. The structure of rare-earth hexaborides in *Pm-3m* symmetry gives the phonon modes of = A$_{1g}$ + E$_g$ + T$_{1g}$ + T$_{2g}$ + 3T$_{1u}$ + T$_{2u}$. The Raman active phonons are A$_g$, E$_g$, and T$_{2g}$, while the optically inactive modes are T$_{2u}$ and T$_{1g}$ and infrared inactive mode is T$_{1u}$ [7, 24]. The peaks located at 766, 1148, and 1280 cm^{-1} indicated the T$_{2g}$, E$_g$, and A1g modes, respectively. Similar results were also reported in the study of
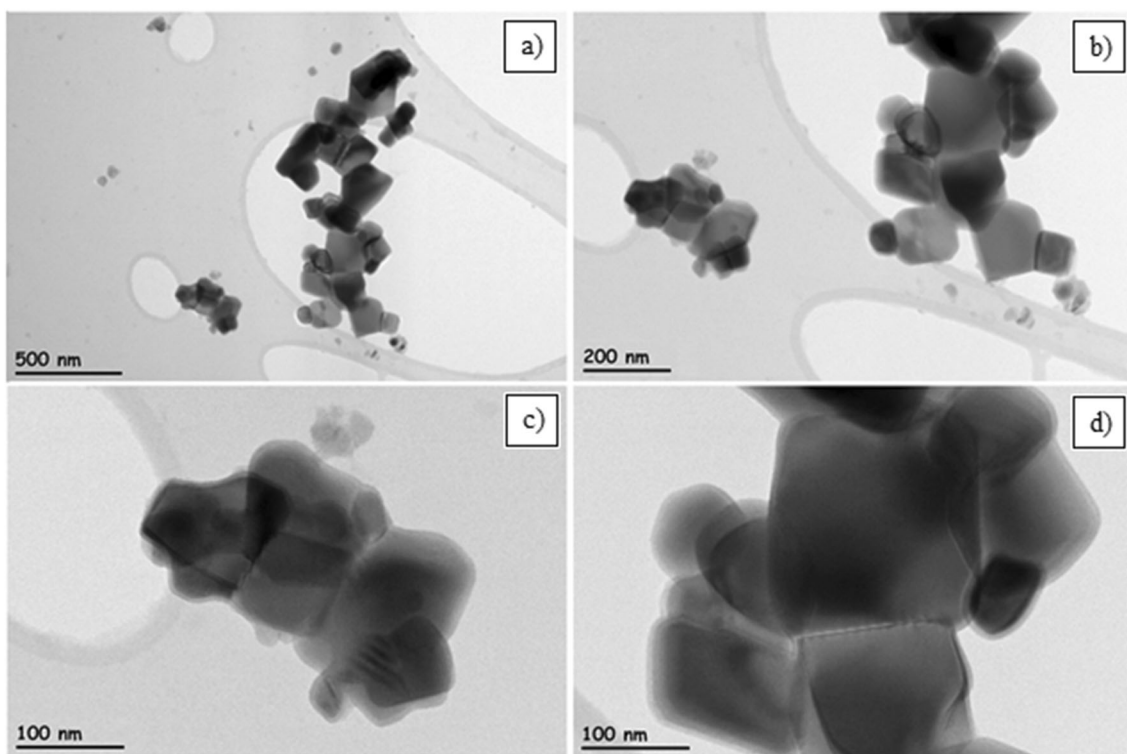
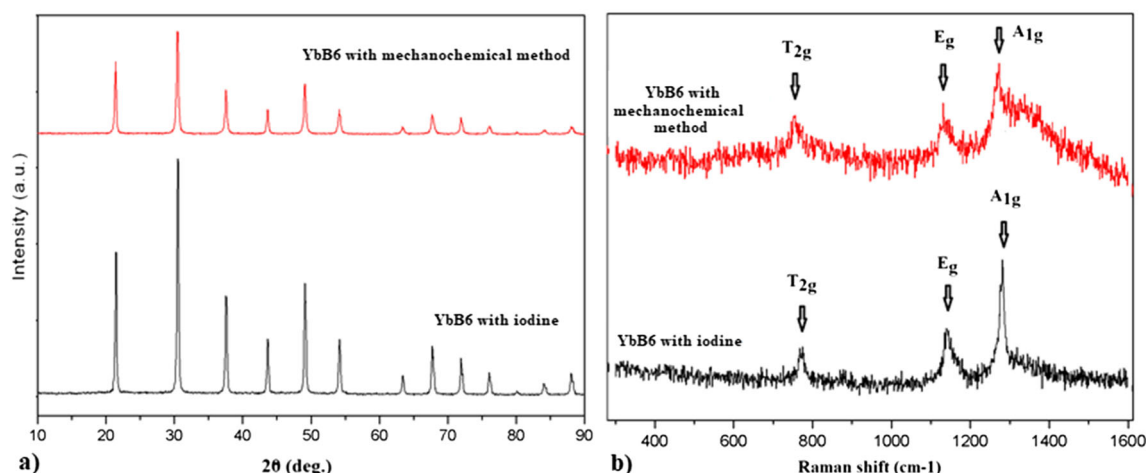**Fig. 8 a–d** HRTEM micrographs of purified YbB$_6$ nanoparticle

Fig. 9 **a** XRD spectra and **b** Raman scattering spectra of purified YbB$_6$ nanoparticle obtained at room temperature with 514 nm excitation and YbB$_6$ with mechanochemical method [13]

Zhou et al. [24]. The basis for the Raman active vibrations is mainly due to the boron octahedra and the position of Yb atom at the inversion center. In another study performed by Ogita et al., the structure of YbB$_6$ was analyzed in detail by Raman spectroscopy [29]. It stated that, due to the displacement of two apical-B atoms, which was twice as those of four planar-B atoms in B$_6$ octahedron, it caused E$_g$ peak to be a doublet. Furthermore, it also mentioned that the line shape of T$_{2g}$ peak indicated symmetry, and no crystal electric field and low energy excitations could be expected at 1400 cm^{-1} [29].

In this context, it is worth mentioning that the physical nature of nano-YbB$_6$ produced by two different methods, viz. present low-temperature reduction method using iodine and mechanochemical method [13], appeared to be different. Despite being chemically the same, YbB$_6$ produced by different methods indicated revealing differences in their morphologies [13]. The XRD peak intensities of the nano-YbB$_6$ synthesized by the mechanochemical means are significantly weaker compared with those of the YbB$_6$ produced by the low-temperature method (Fig. 9a) suggesting less crystallinity or more amorphous in nature. In contrast, sharper high-intensity XRD peaks for nano-YbB$_6$ synthesized by the present low-temperature method using iodine-based reduction method suggests more crystalline in nature. This has been further substantiated by comparing with the Raman peak shifts (T$_{2g}$, E$_g$, and A$_{1g}$) as shown in Fig. 9b. The Raman shifts observed for T$_{2g}$, E$_g$, and A$_g$ peaks are noticeable (Table 5). Their shifts towards higher wave numbers, as tabulated in Table 5 for the nanocrystallites produced by the present

method, indicated the fact that there is a systematic shift of 10–14 cm^{-1} between the YbB$_6$ of the present study versus YbB$_6$ of mechanochemical process. Besides those observed shifts, the Raman peaks for the YbB$_6$ from mechanochemical process were broader and of lower intensity, which can be attributed to the defects and possibly some partial disorders in the lattice structures for the YbB$_6$ produced mechanochemically.

It is of great relevance in this context to highlight some of the most important methods of synthesis of YbB$_6$ used before for the purpose of distinguishing them from the method used in the present study. A summary of the synthetic method used about YbB$_6$ is given in Table 6. From the literature survey, it was noticed that very different method was used for the synthesis of YbB$_6$. The particle size distributions of the synthesized YbB$_6$ varied within the range of 10 μm to 5.5 nm and for the synthesis temperatures varied between 240 and 1750 °C [5, 6, 9–13]. All reported studies as summarized in Table 6 dealt mostly with the bulk YbB$_6$, and a very few studies delineated the synthesis of nano-forms. The lowest temperature studied thus far in those methods was for the synthesis of YbB$_6$ nanowires using heat routed method carried out in an autoclave for 12 h at 240–270 °C. It delineates that, due to the presence of I$_2$ and H$_2$O vapors (about 45 atm), fast transport of Yb and B species can occur under a high-pressure and high-temperature environment, which might have promoted the growth of single crystalline YbB$_6$ nanowires. In another study, synthesis of pure YbB$_6$ of sizes below 40 nm was reported using solid-state metathesis at 650 °C [9]. Very

Table 5 The comparison of Raman active modes (T$_{2g}$, E$_g$, A$_{1g}$) of present study and ref. [13]

Methods	T$_{2g}$	E$_g$	A$_{1g}$
Low-temperature method using I$_2$ (present method)	766 cm^{-1}	1148 cm^{-1}	1280 cm^{-1}
Mechanochemical method [13]	759 cm^{-1}	1134 cm^{-1}	1271 cm^{-1}

Table 6 The studies for synthesis of YbB_6

Reactants	Synthesis method	Product	Reference
Yb-H_3BO_3-Mg-I_2	High-pressure solid-state method, Ar atm., kept at 200–240 °C in autoclave for 12 h, purified by hot HCl sol.	Pure YbB_6 nanowires, diameter 30–200 nm, length 2–10 μm	[5]
Yb_2O_3-B_4C	High-temperature sintering method, Ar atm., kept at 1750 °C for 2 h, no purification	Pure porous YbB_6 particles	[6]
$YbCl_3.6H_2O$-MgB_2	Solid-state metathesis reaction method, Ar atm. kept at 650 °C for 1 h, purified with 5 M HCl sol.	Pure YbB_6 5.5 nm	[9]
Yb_2O_3-amorphous B	Inductive floating zone method, Ar pressure 0.3–1.0 MPa, purified in nitric acid	YbB_6 single crystals	[10]
Chunk Yb-Al-B powders	Al-flux method, Ar atm. kept at 1773 K for 48 h	High-quality YbB_6 single crystals	[11]
$Yb(NO_3)_3.6H_2O$ -CH_6N_4O-B	Combustion synthesis method, kept at 593 K, purified with HCl and H_2SO_4	YbB_6-$YbBO_3$ phases	[12]
Yb_2O_3- Mg-B_2O_3-	Mechanochemical method, Ar atm., purified with HCl sol.	Pure YbB_6 nanocrystals approx. 24 nm	[13]
Yb_2O_3-B_2O_3-Mg-I_2	Combined ball milling and magnesiothermic method, Ar atm., no pressure, kept 85 °C, and purified with HCl sol.	High purity YbB_6 particle size 96 ± 4 nm	This study

recently, the room temperature synthesis of YbB_6 nanocrystals from Yb_2O_3-B_2O_3-Mg powders was firstly achieved at 350 rpm rotating speed via mechanochemical method. The product comprised of irregular shaped nanocrystals with approximately 20 nm [13]. Depending on the methods used, the obtained products can be of nanowire forms, in the form of irregular shaped nanoparticles, or in the form of porous structures [5, 6, 9–13]. The synthesis of porous YbB_6 coarse particles was only reported by Wang et al. by reacting Yb_2O_3-B_4C powder blends at 1750 °C for 2 h [6]. In the literature, longer synthesis time (up to 30 h) revealed the high possibilities of entraining impurities, which were mostly the eventualities of high-temperature and high-pressure synthesis of YbB_6. Their long synthesis time (12–30 h) along with high temperatures and other variables used for those syntheses pointedly differs from the method used for the present study, which involved a simple yet cost-effective experimental setup that enabled synthesizing a very pure nano-form of YbB_6 in a very short period of time (2.5 h milling and approx. 1 h for solid-state reactions) in a most efficient manner. The as-synthesized powder mixtures can easily be purified to form cuboid-shaped nanoparticles successfully.

Conclusion

The synthesis of pure YbB_6 was successfully accomplished by an easy low-temperature experimental setup (85 °C) for Yb_2O_3/B_2O_3/Mg/I_2 powder blends to react under Ar atmosphere. It was seen that mechanical activation and usage of iodine accelerated the synthesis mechanism of YbB_6. The relative percentages of YbB_6, $B_2Mg_3O_6$, MgO, and YbI_2 were determined as $\sim 58\%$, $\sim 26\%$, $\sim 11\%$, and $\sim 5\%$, respectively,

by multi-phase Rietveld refinement technic. It was seen that all intermediate and unwanted phases were successfully removed by 3 M hot aqueous hydrochloric acid solution. The single-phase Rietveld refinement confirmed the cubic structure of YbB_6 in Pm-$3m$ (221) space group with lattice parameters of $a = b = c = 4.143$ Å. TEM images clearly showed the agglomerated, cuboid shapes of purified nanocrystals with the average particle size of 121 ± 5.0 nm. An XRD and Raman comparison of the YbB_6 produced by the present method and by the mechanochemical method revealed that the low-temperature iodine-aided reduction reaction produced highly crystalline phase of the YbB_6 nanoparticles, whereas the mechanochemical method produced less crystalline or more amorphous nanoparticles of YbB_6. Comparison of XRD profiles and Raman active modes (T_{2g}, E_g, and A_{1g}) found around 766, 1148, and 1280 cm^{-1}, respectively, substantiated those inferences.

References

1. Yuan, Y.F., Zhang, L., Liang, L.M., He, K., Liu, R., Min, G.H.: A solid-state reaction route to prepare LaB_6 nanocrystals in vacuum. Ceram. Int. (2011). https://doi.org/10.1016/j.ceramint.2011.03.073

2. Xu, J., Hou, G., Mori, T., Li, H., Wang, Y., Chang, Y., Luo, Y., Yu, B., Ma, Y., Zhai, T.: Excellent field-emission performances of neodymium hexaboride (NdB_6) nanoneedles with ultra-low work

functions. Adv. Funct. Mater. (2013). https://doi.org/10.1002/adfm201301980

3. Selvan, R.K., Genish, I., Perelshtein, I., Moreno, J.M.C., Gedanken, A.: Single step, low-temperature synthesis of submicron-sized rare earth hexaborides. J. Phys. Chem. C. (2008). https://doi.org/10.1021/jp0765502

4. Tanaka, T., Nishitani, R., Oshima, C., Bannai, E., Kawai, S.: The preparation and properties of CeB_6, SmB_6, and GdB_6. J. Appl. Phys. (1980). https://doi.org/10.1063/1.328133

5. Han, W., Wang, Z., Li, Q., Lian, X., Liu, X., Fan, Q., Zhao, Y.: Semiconductor-insulator transition in a YbB_6 nanowire with boron vacancy. J. Solid State Chem. (2018). https://doi.org/10.1016/j.jssc.2018.03.029

6. Wang, X.F., Xiang, H.M., Sun, X., Liu, J.C., Hou, F., Zhou, Y.C.: Porous YbB6 ceramics prepared by in situ reaction between Yb_2O_3 and B_4C combined with partial sintering. J. Am. Ceram. Soc. (2015). https://doi.org/10.1111/jace.13606

7. Ogita, N., Nagai, S., Okamoto, N., Udagawa, M., Iga, F., Sera, M., Akimitsu, J., Kunii, S.: Raman scattering investigation of RB_6 (R=Ca, La, Ce, Pr, Sm, Gd, Dy, and Yb). Phys. Rev. B. (2003). https://doi.org/10.1103/PhysRevB.68.224305

8. Blomberg, M.K., Merisalo, M.J., Korsukova, M.M., Gurin, V.N.: Single-crystal X-ray diffraction study of NdB_6, EuB_6 and YbB_6. J. Alloys Compd. (1995). https://doi.org/10.1016/0925-8388(94)01313-7

9. Aprea, A., Maspero, A., Masciocchi, N., Guagliardi, A., Albisetti, A.F., Giunchi, G.: Nanosized rare-earth hexaborides: low-temperature preparation and microstructural analysis. Solid State Sci. (2013). https://doi.org/10.1016/j.solidstatesciences.2013.04.001

10. Glushkov, V.V., Bozhko, A.D., Bogach, A.V., Demishev, S.V., Dukhnenko, A.V., Filipov, V.B., Kondrin, M.V., Kuznetsov, A.V., Sannikov, I.I., Semeno, A.V., Shitsevalova, N.Y., Voronov, V.V., Sluchanko, N.E.: Bulk and surface electron transport in topological insulator candidate $YbB_{6-\delta}$. Phys. Status Solidi (RRL). (2016). https://doi.org/10.1002/pssr.201510452

11. Xia, M., Jiang, J., Ye, Z.R., Wang, Y.H., Zhang, Y., Chen, S.D., Niu, X.H., Xu, D.F., Chen, F., Chen, X.H., Xie, B.P., Zhang, T., Feng, D.L.: Angle-resolved photoemission spectroscopy study on the surface states of the correlated topological insulator YbB_6. Sci. Rep. (2014). https://doi.org/10.1038/srep05999

12. Kanakala, R., Escudero, R., George, G.R., Ramisetty, M., Graeve, O.A.: Mechanisms of combustion synthesis and magnetic response of high-surface-area hexaboride compounds. ACS Appl. Mater. Interfaces. (2011). https://doi.org/10.1021/am1012276

13. Simsek, T.: Pure YbB_6 nanocrystals: first time synthesis via mechanochemical method. Adv. Powder Technol. (2019). https://doi.org/10.1016/j.apt.2019.03.018

14. Larson, A.C., Dreele, R.B.V.: GSAS: general structure analysis system report LAUR 86–748. Tech. Rep., Los Alamos National Laboratory (2000)

15. Sonnoveld, E.J., Visser, J.W.: Automatic collection of powder data from photographs. J. Appl. Crystallogr. 8, 1–7 (1995). https://doi.org/10.1107/S0021889875009417

16. Williamson, G.K., Hall, W.H.: X-ray line broadening from filed aluminium and wolfram. J Acta Metall. 1, 22–31 (1953)

17. Suryanarayana, C.: Mechanical alloying and milling. Prog. Mater. Sci. (2001). https://doi.org/10.1016/S0079-6425(99)00010-9

18. Baris, M., Simsek, T., Simsek, T., Ozcan, S., Kalkan, B.: High purity synthesis of ZrB_2 by a combined ball milling and carbothermal method: structural and magnetic properties. Adv. Powder Technol. (2018). https://doi.org/10.1016/j.apt.2018.06.024

19. Akçamlı, N., Ağaoğulları, D., Balcı, O., Oveçoğlu, M.L., Duman, I.: Synthesis of HfB_2 powders by mechanically activated borothermal reduction of HfCl4. Ceram. Int. (2016). https://doi.org/10.1016/j.ceramint.2015.11.041

20. Balcı, O., Agaogulları, D., Ovalı, D., Ovecoglu, M.L., Duman, I.: In situ synthesis of NbB_2–NbC composite powders by milling-assisted, carbothermal reduction of oxide raw materials. Adv. Powder Technol. (2015). https://doi.org/10.1016/j.apt.2015.06.001

21. Baris, M., Simsek, T., Akkurt, A.: Mechanochemical synthesis and characterization of pure Co_2B nanocrystals. Bull. Mater. Sci. (2016). https://doi.org/10.1007/s12034-016-1231-x

22. Simsek, T., Baris, M., Kalkan, B.: Mechanochemical processing and microstructural characterization of pure Fe_2B nanocrystals. Adv. Powder Technol. 3056–3062 (2017). https://doi.org/10.1016/j.apt.2017.09.017

23. Wang, L., Xu, L., Ju, Z., Qian, Y.: A versatile route for the convenient synthesis of rare-earth and alkaline-earth hexaborides at mild temperatures. Cryst. Eng. Commun. (2010). https://doi.org/10.1039/c001167c

24. Zhou, Y., Wang, X., Xiang, H., Feng, Z., Wang, G.: Theoretical prediction, preparation, and mechanical properties of YbB_6, a candidate interphase material for future UHTCf/UHTC composites. J. Eur. Ceram. Soc. (2016). https://doi.org/10.1016/j.jeurceramsoc.2016.02.053

25. Zhang, M., Yuan, L., Wang, X., Fan, H., Wang, X., Wu, X., Wang, H., Qian, Y.: A low-temperature route for the synthesis of nanocrystalline LaB_6. J. Solid State Chem. (2008). https://doi.org/10.1016/j.jssc.2007.12.011

26. Besmel, R., Ghaffari, M., Shokrollahi, H., Chitsazan, B., Karimi, L.: Influence of milling time on the structural, microstructural and magnetic properties of mechanically alloyed $Ni_{58}Fe_{12}Zr_{10}Hf_{10}B_{10}$ nanostructured/ amorphous powders. J. Magn. Magn. Mater. (2011). https://doi.org/10.1016/j.jmmm.2011.05.025

27. Amini, R., Hadianfard, M.J., Salahinejad, E., Marasi, M., Sritharan, T.: Microstructural phase evaluation of high-nitrogen Fe–Cr–Mn alloy powders synthesized by the mechanical alloying process. J. Mater. Sci. (2009). https://doi.org/10.1007/s10853-008-3117-9

28. Abbasi, S., Eslamizadeh, H., Raanaei, H.: Study of synthesis, structural and magnetic properties of nanostructured $(Fe_{67}Ni_{33})_{70}Ti_{10}B_{20}$ alloy. J. Magn. Magn. Mater. (2018). https://doi.org/10.1016/j.jmmm.2017.12.015

29. Ogita, N., Nagai, S., Okamoto, N., Iga, F., Kunii, S., Akamtsu, T., Akamtsu, T., Akimitsu, J., Udagawa, M.: Raman scattering study of CaB_6 and YbB_6. J. Solid State Chem. 177 (2004). https://doi.org/10.1016/j.jssc.2003.02.014